Cite this: *J. Mater. Chem. A*, 2021, 9, 23477

Crystalline mixed-valence copper supramolecular isomers for electroreduction of CO₂ to hydrocarbons†

Jia-Ni Lu,^a Jiang Liu,^{*a} Lei Zhang,^a Long-Zhang Dong,^{id}^a Shun-Li Li^{*a} and Ya-Qian Lan^{id}^{*ab}

Supramolecular isomers can serve as effective model systems to explore the stable self-assembly process of specific structures, but it is often difficult to capture multiple variants in different stable states. Here, four variants (CuL-1, CuL-2, CuL-3, and CuL-4) assembled from the same Cu^ICu^{II}L-metallogand motif form different structures in which the dihedral angles of adjacent Cu^ICu^{II}L-metallogands (9°, 33°, 84°, 180°) increase gradually. CuL-2, CuL-3 and CuL-4 belong to supramolecular isomers. The relevant experimental and calculative results demonstrate that the larger the dihedral angle of adjacent Cu^ICu^{II}L-metallogands, the higher the stability of the structural variant. Moreover, the metastable structures (CuL-1, CuL-2, and CuL-3) can undergo single crystal-to-single crystal transformation into the most stable variant (CuL-4). Additionally, based on the unique mixed-valence copper structure distribution characteristics and strong alkali stability, CuL-4 is applied as an electrocatalyst for CO₂ electroreduction (CO₂RR), in which CO₂ can be reduced to high-value hydrocarbons with a total faradaic efficiency of 85.02% (FE_{CH₄} = 67.76%, FE_{C₂H₄} = 17.26%) at -1.0 V (*j* = 477.42 mA cm⁻²). As far as we know, CuL-4 is better than most crystalline CO₂RR catalysts. Furthermore, the corresponding DFT calculation proves that the independent Cu(I) sites are mainly responsible for CH₄ generation, while the synergistic two adjacent Cu(II) sites are inclined to produce C₂H₄. Significantly, crystalline CuL-4 can serve as a well-defined model electrocatalyst to explore the role of evenly distributed mixed-valence copper active sites in reducing CO₂ to hydrocarbons.

Received 21st August 2021
Accepted 22nd September 2021

DOI: 10.1039/d1ta07148c

rsc.li/materials-a

Introduction

Coordination compounds are crystalline materials in which metal ions/metal clusters and organic ligands are connected by coordination bonds.¹ Their well-defined and adjustable structures²⁻⁴ are conducive to the study of the specific physicochemical property and reaction mechanism at the atomic level. Therefore, in recent years, coordination compounds have shown great potential in many fields like catalysis,⁵⁻⁹ sensing,^{10,11} drug delivery,^{12,13} gas storage and separation,^{14,15} and so on. In addition, through a flexible self-assembly process, the same reaction components can be used to construct isomeric coordination compounds (named supramolecular

isomers)^{16,17} with different structural conformations. Although there are usually only slight structural changes among different variants of supramolecular isomerism, significant differences in physicochemical properties often occur. Especially the impact on their structural stability generally directly determines their potential application. Significantly, for the supramolecular isomeric system, the huge challenge is the structure capture of unstable variants, because the rotation or twisting of metal ions/clusters,¹⁸⁻²¹ the flexibility^{22,23} or chirality^{24,25} changes of organic linkers, as well as the dislocation,²⁶ packing,²⁷ interpenetration^{28,29} of frameworks, often greatly reduce their crystallinity and structural stability.

Generally, it is very normal for isomeric coordination compounds to produce different structural variants in the thermodynamic or kinetic self-assembly process. Moreover, these structural variants in many cases are very important to understand the specific structure–property relationship and reaction mechanism. But it is often difficult to effectively capture many of the regular structural variants, because the effective crystallization of different structural variants by the targeted regulation of the growth environment of the specific compound still needs to consider a lot of main factors such as: (i) the regularity of reaction conditions such as the influence of

^aJiangsu Collaborative Innovation Centre of Biomedical Functional Materials, Jiangsu Key Laboratory of New Power Batteries, School of Chemistry and Materials Science, Nanjing Normal University, Nanjing 210023, P. R. China. E-mail: yqlan@njnu.edu.cn; liuj@njnu.edu.cn; slli@njnu.edu.cn

^bSchool of Chemistry, South China Normal University, Guangzhou, 510006, P. R. China. E-mail: yqlan@m.scnu.edu.cn; Web: <http://www.yqlangroup.com>

† Electronic supplementary information (ESI) available: Experimental methods and supporting figures and tables. CCDC 2079540–2079543. For ESI and crystallographic data in CIF or other electronic format see DOI: 10.1039/d1ta07148c

pH,³⁰ the ratio of the metal salt to ligand, solvent^{20,31–33} and temperature,^{27,34–36} (ii) modulators added to control the directional growth of the crystal,^{37–39} and (iii) the serendipity and accidental errors in the process of solvothermal synthesis. These considerations are extremely crucial for the discovery and in-depth study of a supramolecular isomerism system.

In this work, we discover a thermodynamically induced isomeric coordination compound system, in which four different structural variants with mixed-valence copper ions, molecular $\text{Cu}^{\text{I}}_3\text{Cu}^{\text{II}}_3(\text{NO}_3)_3\text{L}_3$ (**CuL-1**, $\text{H}_2\text{L} = N,N'$ -(propane-1,3-diyl)bis(1-(1*H*-imidazol-4-yl)methanimine)) and layered $\text{Cu}^{\text{I}}\text{Cu}^{\text{II}}_2\text{L}_2$ (**CuL-2**, **CuL-3**, and **CuL-4**), are successfully captured. These four compounds are self-assembled with the same $\text{Cu}^{\text{I}}\text{Cu}^{\text{II}}\text{L}$ -metalloligand structural motif which represents a H_2L ligand connecting a couple of $\text{Cu}(\text{I})$ and $\text{Cu}(\text{II})$ ions (Fig. 1). But the difference is that the dihedral angles of the two adjacent $\text{Cu}^{\text{I}}\text{Cu}^{\text{II}}\text{L}$ -metalloligands are gradually increasing (9° , 33° , 84° , 180°). **CuL-1** (9°) is a zero-dimensional single molecule while **CuL-2** (33°), **CuL-3** (84°), and **CuL-4** (180°) are the two-dimensional layered structures formed by different packing patterns. Among them, **CuL-2**, **CuL-3**, and **CuL-4** constitute a supramolecular isomeric system. The calculation results prove that as the dihedral angle increases, the energy decreases, which means that the structural stability of the isomerized **CuL-2**, **CuL-3**, and **CuL-4** is higher and higher. Moreover, the chemical stability results also show that the stability sequence of these three compounds is: **CuL-4** > **CuL-3** > **CuL-2**. It is worth noting that **CuL-1**, **CuL-2**, and **CuL-3** can also be successfully converted into the most stable variant (**CuL-4**) by single crystal-to-single crystal (SCSC) transformation through regulating the thermodynamic synthesis conditions.

Additionally, in view of the fact that stable Cu-based catalyst materials have been widely proven to be effective for the CO_2 electroreduction reaction (CO_2RR),^{40–43} we speculate that **CuL-4** with high chemical stability and uniformly distributed mixed-valence Cu ions probably has the potential to be the catalyst for this reaction. Interestingly, **CuL-4** exhibits a high faradaic efficiency of 85.02% for hydrocarbons ($\text{FE}_{\text{CH}_4} = 67.76\%$, $\text{FE}_{\text{C}_2\text{H}_4} = 17.26\%$) with a current density of $477.42 \text{ mA cm}^{-2}$ for the CO_2RR at -1.0 V vs. RHE , outperforming most crystalline

CO_2RR catalysts. Furthermore, density functional theory (DFT) calculation results reveal that the isolated $\text{Cu}(\text{I})$ sites are the primary catalytic sites for the overall CO_2RR and tend to produce CH_4 , while the two spatially closest $\text{Cu}(\text{II})$ sites can synergistically induce the production of C_2H_4 . This work provides a well-defined structural model to study the function of mixed-valence copper catalytic sites in the electroreduction of CO_2 to hydrocarbons.

Results and discussion

Structure and characterization

At first, we synthesized and collected blue block-shaped crystals (**CuL-1**) in the DMF/MeOH mixed solvent using a simple solvothermal method. Single-crystal X-ray diffraction analysis reveals that **CuL-1** as a single molecule crystallizes in triclinic space group $P\bar{1}$, and its asymmetric unit includes three Cu^{II} ions, three Cu^{I} ions, three L^{2-} ligands, and three NO_3^- ions (Fig. S2†). As shown in Fig. S4–S5†, **CuL-1** contains two types of copper ions in different valence states. The monovalent Cu ions linearly coordinate two H_2L ligands. The divalent Cu ions exhibit the tetragonal pyramid coordination geometry, with four imidazole N from the same H_2L ligand coordinated on the bottom and one NO_3^- ion coordinated axially. And the dihedral angle of two adjacent $\text{Cu}^{\text{I}}\text{Cu}^{\text{II}}\text{L}$ -metalloligands (planes A and B) connected to the Cu^{I} ion is 9° (Fig. 2a). Simply speaking, **CuL-1** with a triangular molecular structure is connected head-to-tail by three $\text{Cu}^{\text{I}}\text{Cu}^{\text{II}}\text{L}$ -metalloligands (Fig. 2e). The three-dimensional supramolecular compound is formed by packing molecules probably due to the weak $\text{C-H}\cdots\text{O}$ interactions ($\text{H}\cdots\text{O}$ bond distance of $2.478\text{--}2.912 \text{ \AA}$, Fig. S6†). And each molecule has six nearest neighbors (Fig. S7†).

In the process of exploring the reaction conditions, we obtained three 2D layered structures (**CuL-2**, **CuL-3** and **CuL-4**) by replacing HNO_3 with Et_3N . We find that the molar ratio of the

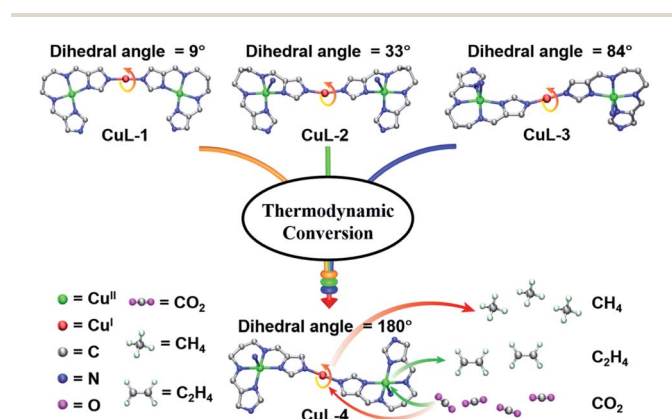


Fig. 1 The stable self-assembly process of **CuL-*n*** ($n = 1, 2, 3, 4$) consisting of the same $\text{Cu}^{\text{I}}\text{Cu}^{\text{II}}\text{L}$ -metalloligand motifs.

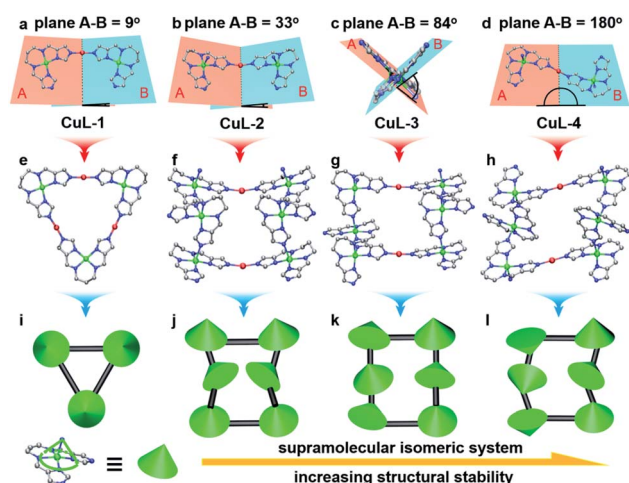


Fig. 2 (a–d) The dihedral angle of two adjacent $\text{Cu}^{\text{I}}\text{Cu}^{\text{II}}\text{L}$ -metalloligands (planes A and B) in **CuL-1** (a), **CuL-2** (b), **CuL-3** (c), and **CuL-4** (d), (e) the single molecule structure of **CuL-1**, (f–h) the single layer structure of **CuL-2** (f), **CuL-3** (g), and **CuL-4** (h), and (i–l) the simplified structural diagram of **CuL-1** (i), **CuL-2** (j), **CuL-3** (k), and **CuL-4** (l).

metal salt ($\text{CuCl}_2 \cdot 2\text{H}_2\text{O}$) and the ligand (H_2L) and the mixed solvent are the two main influencing factors. When the molar ratio of $\text{CuCl}_2 \cdot 2\text{H}_2\text{O}$ and H_2L is increased from 1.25 : 1 to 6 : 1, the product changes from **CuL-2** to **CuL-3**. And when the mixed solvent of $\text{H}_2\text{O}/\text{MeOH}$ is used instead of DMF/MeOH , the product changes from **CuL-3** to **CuL-4**.

Single-crystal X-ray diffraction analysis reveals that **CuL-2**, **CuL-3**, and **CuL-4** crystallize in orthorhombic space group $Pnma$, monoclinic space group $C2/c$, and monoclinic space group $P2_1/c$, respectively. All of their asymmetric units contain a Cu^{II} ion, a Cu^{I} ion, and an L^{2-} ligand (Fig. S8†). In these three structures, there are two different valence states of copper ions. The Cu^{I} ion adopts a linear coordination geometry with two N atoms on the imidazole from different ligands (Fig. S10†). The Cu^{II} ion with quadrangular pyramid coordination geometry is coordinated with four N atoms from the same H_2L ligand and one N atom on the imidazole from another H_2L ligand (Fig. S11†). Furthermore, they have similar basic units ($\text{Cu}^{\text{I}}\text{Cu}^{\text{II}}\text{L}$ -metalloligand), the same as **CuL-1**. Because of the rotatable character of the single bond, the dihedral angles of planes A and B can be changed along with the rotation of the $\text{Cu}^{\text{I}}\text{-N}$ bond. Fig. 2b–d show that the dihedral angles of planes A and B in **CuL-2**, **CuL-3**, and **CuL-4** are 33° , 84° , and 180° , respectively. The ligands and the metal ions are connected to each other in the above manner to form further different 2D layered structures, namely **CuL-2**, **CuL-3**, and **CuL-4** (Fig. 2f–h). Besides, considering the $\text{Cu}^{\text{I}}\text{Cu}^{\text{II}}\text{L}$ -metalloligands as 3-connected sites, the frameworks of these three isomeric coordination polymers share the same Schläfli symbol of 6^3 and topological type named the *hcb* code (Fig. S12–S14†). So, omitting counterions and solvent molecules, **CuL-2**, **CuL-3**, and **CuL-4** share the same formula as a result that they are supramolecular isomers. As seen in Fig. S15–S17,† it showed the layered packing of **CuL-2**, **CuL-3**, and **CuL-4** and the layer spacing of these crystals are 7.856 Å, 7.207 Å, and 8.685 Å, respectively.

The powder X-ray diffraction (PXRD) patterns of **CuL-1**, **CuL-2**, **CuL-3**, and **CuL-4** are well matched with their simulated peaks, which prove that these compounds have high purity and good crystallinity, as shown in Fig. S18–S21.† Thermogravimetric analysis (TGA, Fig. S23†) shows that **CuL-1** is thermally stable below 280°C while the three supramolecular isomers have higher thermal stability and are stable until 320°C . After that, we use X-ray photoelectron spectroscopy (XPS) to analyse the elements contained in the material and the corresponding valence states. The XPS survey patterns uncover the existence of Cu, C, N, and O in **CuL-1** and Cu, C, N, O, and Cl in the other crystals (Fig. S24†). As shown in Fig. S25d† about **CuL-4**, the $\text{Cu } 2p_{3/2}$ peak can be divided into two components. Binding energies at 934.09 eV and 932.01 eV belong to $\text{Cu}(\text{II})$ and $\text{Cu}(\text{I})$ ions. And the deconvolution of the $\text{Cu } 2p_{1/2}$ peak can be assigned to the $\text{Cu}(\text{II})$ (953.94 eV) and $\text{Cu}(\text{I})$ (951.55 eV), respectively. The XPS spectra of the other three compounds are similar to that of **CuL-4**, which all prove their characters of the mixed-valence copper.

Chemical stability

PXRD characterization of four compounds after immersing for 24 hours in H_2O or KOH aqueous solution with different pH

values reveals that **CuL-2** is unstable in water while **CuL-1** and **CuL-3** can remain stable at $\text{pH} = 12$ and $\text{pH} = 10$, respectively. It is worth noting that the PXRD pattern of **CuL-4** has not undergone any obvious changes no matter it is soaked in 1 M KOH, 5 M KOH, or even 10 M KOH for 24 hours, which fully proves that **CuL-4** has the highest alkali tolerance among these four compounds. And the order of alkaline stability for supramolecular isomers is **CuL-4** > **CuL-3** > **CuL-2**. Moreover, we also find that by regulating specific reaction conditions, **CuL-1**, **CuL-2**, and **CuL-3** can be converted to **CuL-4** by SCSC transformation. When the three crystals (**CuL-1**, **CuL-2**, and **CuL-3**) are kept in a mixed solvent of DMF and H_2O at 120°C for three days, we successfully obtain green diamond shape crystals (**CuL-4**). Therefore, we hold the opinion that stark differences in chemical stability result from small geometric changes of structure. Since the significant difference in the structural composition of isomeric **CuL-2**, **CuL-3**, and **CuL-4** is that the dihedral angle of planes A and B increases gradually, we guess that their structural isomerization may lead to their different stability.

For the purpose of proving this hypothesis, we carry out DFT calculations through a well-defined crystal structure as the model. We choose the fixed $\text{Cu}^{\text{I}}\text{Cu}^{\text{II}}\text{L}$ -metalloligand (plane A) and change the adjacent $\text{Cu}^{\text{I}}\text{Cu}^{\text{II}}\text{L}$ -metalloligand (plane B) by rotating the $\text{Cu}^{\text{I}}\text{-N}$ single bond to obtain the single-layer structure of **CuL-2** (planes A and B = 33°), **CuL-3** (planes A and B = 84°), and **CuL-4** (planes A and B = 180°). The calculation results (Fig. S26†) show that **CuL-4** with a dihedral angle of 180° has the lowest energy and is defined as 0 eV. When the dihedral angle decreases to 84° , the energy increases by 0.35 eV, and when the dihedral angle continues to decrease to 33° , the energy is increased to 1.51 eV. Based on the theory that the relative energy is inversely proportional to thermodynamic stability, we infer that the thermodynamic stability order of these structures is **CuL-4** > **CuL-3** > **CuL-2**, which is consistent with the experimental results. The possible reason for this phenomenon is that as the dihedral angle of the planes A and B increases, the distance between the adjacent $\text{Cu}^{\text{I}}\text{Cu}^{\text{II}}\text{L}$ -metalloligands directly connected to the $\text{Cu}(\text{II})$ atoms of the metalloligands A and B becomes larger and larger, resulting in a decrease in the steric hindrance between them, thereby enhancing the stability of the structure.

Electrocatalytic performance

In view of the excellent chemical stability and the structural character of the mixed-valence copper of **CuL-4**, the exploration of its specific applications is also very important. As we all know, copper-based electrocatalyst materials have been proven to exhibit outstanding catalytic activity in the CO_2RR .^{44–46} Especially for the production of high-value hydrocarbon reduced products, they often show high faradaic efficiency and current density.^{47–50} The application of well-defined crystalline material catalysts in the CO_2RR can provide a lot of important and intuitive evidence for the accurate identification of the real catalytically active sites and the study of the reaction mechanism. However, there are still very few reported cases of crystalline material electrocatalysts used in the CO_2RR .^{51–53} In

addition, it is worth noting that mixed-valence copper can regulate the products of the CO₂RR and shows good performances in the CO₂RR,^{54–56} but there is still a lack of effective structural model systems to study the relevant catalytic reaction mechanism. Therefore, if **CuL-4** with excellent structural chemical stability and exposed mixed-valence copper sites can be used as an electrocatalyst for the CO₂RR, it may provide some opportunities and insights for solving the above problems. The electrocatalytic properties of **CuL-4** toward the CO₂RR are evaluated using a flow cell in 1 M KOH electrolyte. The flow cell can feed gaseous CO₂ directly to the electrode–electrolyte interface, thereby avoiding the limitation of CO₂ transmission. All potentials are referenced to a reversible hydrogen electrode (RHE) and the current density is calculated based on the geometric surface area of the electrode.

In order to test the reaction activity of **CuL-4**, linear sweep voltammetry (LSV) is performed under CO₂/Ar atmospheres at a scan rate of 5 mV s⁻¹ in 1 M KOH. As shown in Fig. 3a, LSV curves show that **CuL-4** under the CO₂ atmosphere has a lower onset potential and higher current density than that under Ar flow, indicating that **CuL-4** has stronger catalytic performance for the CO₂RR rather than the HER. To monitor CO₂RR products of **CuL-4**, we perform chronoamperometric measurements at different potentials. And the gaseous products are detected using gas chromatography (GC) and the liquid products are

analysed *via* proton nuclear magnetic resonance spectroscopy (¹H-NMR). The gas chromatograms (Fig. S27†) show the presence of CO, CH₄, C₂H₄, and H₂ in the product, while the spectrum of ¹H-NMR (Fig. S28†) clearly proves that there are scarcely any liquid products.

The faradaic efficiencies of HER, CO₂RR and hydrocarbons at different potentials are summarized in Fig. 3b. Obviously, FE_{CO₂RR} in a wide potential range from -0.6 to -1.1 V exceeds 70%, much higher than FE_{HER}, which indicates that the HER as a competitive reaction is inhibited with **CuL-4** as the catalyst. At the same time, hydrocarbons become the main product of the CO₂RR at the potentials of ≥ -0.8 V. And the highest FE of hydrocarbons is 85.02% at -1.0 V. In detail, Fig. 3c and Table S10† show the FE of different CO₂RR products. It is found that the FE of H₂ is as high as 75.37% at -0.5 V ($j = 18.27 \text{ mA cm}^{-2}$), so H₂ is the main product at low potential. At -0.6 V ($j = 47.59 \text{ mA cm}^{-2}$), H₂ production decreases, while CO production increases and becomes the main product (FE_{CO} = 57.46%). As the potential continues to increase, the output of H₂ and CO gradually falls off, enhancing the production rates of CH₄ and C₂H₄. This trend indicates that under high overpotential, by further converting the CO adsorbed on the catalyst surface, the production of CH₄ and C₂H₄ can be promoted. Therefore, C₂H₄ becomes the main product (FE_{C₂H₄} = 31.85%) at -0.7 V ($j = 124.84 \text{ mA cm}^{-2}$) and CH₄ is the principal product at higher potential (-0.8–-1.1 V). Specifically, **CuL-4** gives the highest FE_{CH₄} value (67.76%) at -1.0 V with a high current density of 477.42 mA cm⁻², accompanied by a small amount of co-production of H₂ (FE = 7.75%), CO (FE = 4.89%), and C₂H₄ (FE = 17.26%). Moreover, the partial current density of CH₄ (j_{CH_4}) and turnover frequency of CH₄ (TOF_{CH₄}) increase stage by stage with the potential continuously increasing (from -0.5 V to -1.1 V). And at -1.0 V, j_{CH_4} of **CuL-4** is 312.77 mA cm⁻² while TOF_{CH₄} of **CuL-4** is 944.03 h⁻¹ (Fig. 3d). So, for **CuL-4**, -1.0 V is the best potential for applications, and the performance of **CuL-4** is better than most of the CO₂RR crystalline electrocatalysts (Table S11†).

In order to further prove the carbon source of the product, we carry out an isotope calibration test under the ¹³CO₂ atmosphere, and the gas phase products are collected and detected by GC-MS. Mass spectra (Fig. 3e–f and S30†) clearly show the presence of ¹³CH₄ ($m/z = 17$), ¹³C₂H₄ ($m/z = 30$), and ¹³CO ($m/z = 29$), fully proving that the carbon in the CO₂RR product comes from CO₂. And the measurement proves that bare carbon paper cannot electrocatalyze CO₂ reduction (Fig. S31†). For the purpose of analysing the electrochemical stability of **CuL-4**, a long-term durability test is conducted at -1.0 V by the chronoamperometry test. In this process, **CuL-4** can keep a stable current density and maintain values of FE_{CH₄} above 60% within 3600 s (Fig. S32†). The results show that **CuL-4** can retain both activity and selectivity during the CO₂RR process. The PXRD spectra (Fig. S33†) and Cu 2p XPS patterns (Fig. S34†) of **CuL-4** after catalysis are nearly the same as those before the test, revealing that **CuL-4** hardly changes during the catalytic reaction. Besides, the ICP and ICP-MS analyses of solution after electroreduction (-1.0 V) of CO₂ for **CuL-4** further prove the stability of the catalyst (Table S12†).

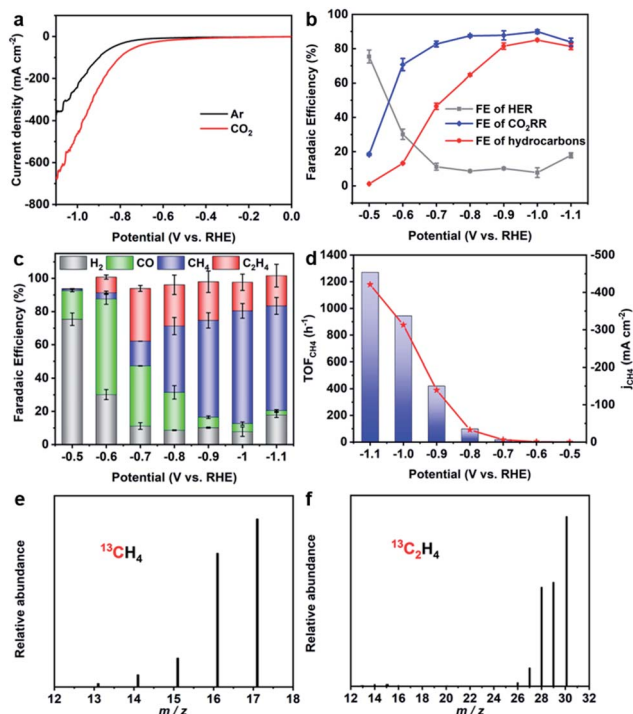


Fig. 3 (a) Linear sweep voltametric curves of **CuL-4**, (b) faradaic efficiencies of **CuL-4** for the HER, total CO₂RR, and hydrocarbons, (c) faradaic efficiencies of **CuL-4** for H₂, CO, CH₄, and C₂H₄ at different applied potentials, (d) the turnover frequency and partial current density of CH₄ at different applied potentials, (e) mass spectra extracted from GC-MS analysis of the CH₄ product from ¹³CO₂ reduction, (f) mass spectra extracted from GC-MS analysis of the C₂H₄ product from ¹³CO₂ reduction.

DFT calculations

Based on the well-defined crystalline structure model (**CuL-4**), DFT calculation is carried out to identify the role of mixed-valence copper catalytic sites during the process of CO₂ electroreduction to hydrocarbons. Previous studies demonstrate that *CO serves as a key intermediate for further reduction products of CH₄ and C₂H₄.^{57,58} From Fig. 3c, it can be noticed that the concentration of CO decreases with the increase of CH₄ production, confirming that the *CO production plays a key role in the further reduction processes. Based on the free energy diagram in Fig. 4a, the rate-determining steps (RDS) of CO production on Cu(I) and Cu(II) sites are different from each other. The Cu(I) sites can activate CO₂ effectively with a decreased free energy change of *COOH and the breakage of the C–O bond for H₂O production requires an energy barrier of 0.36 eV. For Cu(II) sites, the first hydrogenation process needs an energy barrier of 0.88 eV and the second hydrogenation step follows with decreased free energy change. The large energy barrier required on Cu(II) sites indicates that the reaction rate is much slower than that on Cu(I) sites, and thus Cu(I) sites are considered as the primary reaction sites for the overall CO₂RR. In the following, the CH₄ production on both Cu(I) and Cu(II) sites proceeds with multiple proton coupled electron transfer processes, *CO→*CHO→*CHOH→*CH₂OH→*CH₂→*CH₃→*CH₄ (Fig. 4a and Table S13[†]). In particular, the RDS for CH₄ after *CO is the *CH₂ formation with the second C–O bond breakage and the release of a second H₂O molecule. Again, the Cu(I) sites present higher reaction activity for CH₄ production with a free

energy barrier of 0.86 eV compared with Cu(II) sites of 1.34 eV. However, the production of C₂H₄ on Cu(I) sites is unlikely due to the long distance between adjacent Cu(I)–Cu(I) sites (8.685 Å) as shown in Fig. S37.† In contrast, the adjacent Cu(II) sites with a synergetic effect can promote the C–C coupling ground on the Cu(II)–Cu(II) distance of 4.447 Å. As shown in Fig. 4b, the energy barrier of C–C coupling is 0.95 eV, which is considered as the potential determining step. The *COCO intermediate is then further stepwise reduced to *COCHO, *COCH₂O, *COHCH₂O, *CHOHCH₂O, and *CHCH₂O. *CHCH₂O causes the final H⁺/e[−] hydrogenation and further desorbs to form *O and C₂H₄. Therefore, the Cu(I) sites play an essential role in the overall CO₂RR and the reduction products are dominated by CH₄ with the suitable potential applied, while synergetic two adjacent Cu(II) sites contribute to the C₂H₄ production and the reaction rate is slow due to that the large energy barrier is required.

Conclusions

In summary, we design and synthesize four mixed-valence copper compounds (**CuL-1**, **CuL-2**, **CuL-3**, and **CuL-4**) with the Cu^ICu^{II}L-metalloligand as the structural motif. Among them, the alkaline stability of the supramolecular isomers (**CuL-2**, **CuL-3**, and **CuL-4**) enhances with the increase of the dihedral angle of two adjacent Cu^ICu^{II}L-metalloligands, which has been proved by the relevant experimental and calculation results. In addition, the metastable **CuL-1**, **CuL-2**, and **CuL-3** can be converted to stable **CuL-4** through SCSC transformation by regulating thermodynamic synthesis conditions. Based on the strong alkali tolerance and the structural character of mixed-valence copper, **CuL-4** is further applied in the CO₂RR, and it can reduce CO₂ to hydrocarbons with a high FE of 85.02% (FE_{CH₄} = 67.76%, FE_{C₂H₄} = 17.26%) at −1.0 V vs. RHE, and the current density is as high as 477.42 mA cm^{−2}. The DFT calculations reveal that the independent Cu(I) sites tend to catalyze the production of CH₄, and two adjacent Cu(II) sites with a closer distance have a synergistic effect for C–C coupling to obtain C₂H₄. This work represents a model system to prove the stable self-assembly process of isomeric compounds by regulating the dihedral angle of the structural component. Also, **CuL-4**, as the stable crystalline electrocatalyst, provides an important case study to survey the influence of the catalytically active mixed-valence copper sites on the electroreduction of CO₂ to hydrocarbons.

Experimental section

Synthesis of *N,N'*-(propane-1,3-diyl)bis(1-(1*H*-imidazol-4-yl)methanimine) (**H₂L**)

H₂L was synthesized based on the literature method.⁵⁹ A methanol solution (40 mL) of 1,3-diaminopropane (2.964 g, 40 mmol) was added to a methanol solution (100 mL) of 1*H*-imidazole-4-carbaldehyde (7.688 g, 80 mmol). The mixture was stirred 12 h at 50 °C. A product of light-yellow powder (**H₂L**) was obtained by rotary evaporation (1.624 g, yield 70.61%).

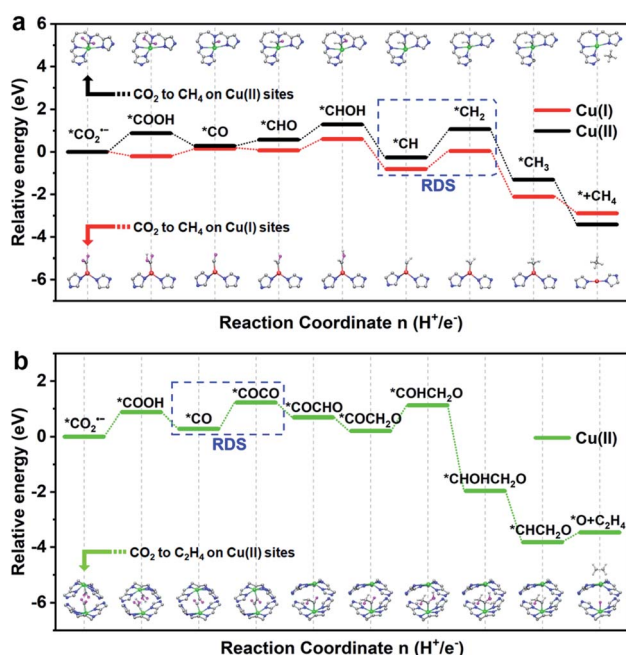


Fig. 4 (a) Calculated free energy diagram and the corresponding intermediates for CO₂ electrocatalytic reduction to CH₄ on the Cu(I) sites and Cu(II) sites of the **CuL-4** model catalyst, (b) calculated free energy diagram and the corresponding intermediates for CO₂ electrocatalytic reduction to C₂H₄ on the Cu(II) sites of the **CuL-4** model catalyst.

Synthesis of CuL-1

H₂L (0.0092 g, 0.04 mmol) and CuCl₂·2H₂O (0.041 g, 0.24 mmol) were dissolved in a mixture solution of DMF (2 mL) and MeOH (2 mL) by ultrasonication, followed by mixing with HNO₃ (90 μL). Subsequently, the mixture solution was transferred into a 10 mL glass vial for 72 h at 100 °C under autogenous pressure. After cooling down to room temperature, the blue block-shaped crystals were collected by filtration and washed with DMF and MeOH.

Synthesis of CuL-2

H₂L (0.0092 g, 0.04 mmol) and CuCl₂·2H₂O (0.0085 g, 0.05 mmol) were dissolved in a mixture solution of DMF (2.5 mL) and MeOH (3.5 mL) by ultrasonication, followed by mixing with Et₃N (45 μL). Subsequently, the mixture solution was transferred into a 10 mL glass vial for 72 h at 100 °C under autogenous pressure. After cooling down to room temperature, the green sheet crystals were collected by filtration and washed with DMF and MeOH.

Synthesis of CuL-3

H₂L (0.0092 g, 0.04 mmol) and CuCl₂·2H₂O (0.041 g, 0.24 mmol) were dissolved in a mixture solution of DMF (3 mL) and MeOH (1 mL) by ultrasonication, followed by mixing with Et₃N (60 μL). Subsequently, the mixture solution was transferred into a 10 mL glass vial for 72 h at 100 °C under autogenous pressure. After cooling down to room temperature, the green sheet crystals were collected by filtration and washed with DMF and MeOH.

Synthesis of CuL-4

H₂L (0.0092 g, 0.04 mmol) and CuCl₂·2H₂O (0.041 g, 0.24 mmol) were dissolved in a mixture solution of H₂O (3 mL) and MeOH (1 mL) by ultrasonication, followed by mixing with Et₃N (80 μL). Subsequently, the mixture solution was transferred into a 10 mL glass vial for 72 h at 100 °C under autogenous pressure. After cooling down to room temperature, the green sheet crystals were collected by filtration and washed with H₂O and MeOH.

Thermodynamic conversion of CuL-1 to CuL-4

5.0 mg of CuL-1 crystals was added into a mixture solution of DMF (5 mL) and H₂O (1 mL) and then transferred into a 10 mL glass vial for 72 h at 120 °C under autogenous pressure. After cooling down to room temperature, green diamond shape crystals of CuL-4 were obtained and collected by filtration.

Thermodynamic conversion of CuL-2 or CuL-3 to CuL-4

5.0 mg of CuL-2 or CuL-3 crystals was added into a mixture solution of DMF (3 mL) and H₂O (1 mL) and then transferred into a 10 mL glass vial for 72 h at 120 °C under autogenous pressure. After cooling down to room temperature, green diamond shape crystals of CuL-4 were obtained and collected by filtration.

Characterization and instruments

Powder X-ray diffraction (PXRD) spectra were recorded on a Rigaku D/Max 2500/PC diffractometer equipped with graphite

monochromatized Cu K α radiation ($\lambda = 1.54060 \text{ \AA}$) at 40 kV and 100 mA. Fourier transform infrared spectroscopy (FT-IR) was performed on a NEXUS670 using the KBr pellet in the range of 4000–400 cm⁻¹. Thermogravimetric analyses (TGA) were carried out on a PerkinElmer Diamond DSC Pyris analyser under oxygen with a heating rate of 10 °C min⁻¹ from room temperature to 800 °C. X-ray photoelectron spectra (XPS) were recorded using an Escalab 250Xi instrument from Thermo Scientific equipped with an Al K α microfocused X-ray source and the C 1s peak at 284.6 eV as the internal standard. ¹H-NMR was carried out on an AVANCE III 400M spectrometer (Bruker). Single-crystal XRD data of crystals were measured on a Bruker APEX II CCD diffractometer with graphite-monochromated Mo K α radiation ($\lambda = 0.71073 \text{ \AA}$) at 296 K. All the structures were solved by the direct method using the SHELX-2014 program and refined on Olex-2 software. The detailed crystallographic information of these crystals is listed in Table S1.† The CCDC numbers of CuL-1, CuL-2, CuL-3, and CuL-4 are 2079542, 2079541, 2079540, and 2079543.

Electrochemical measurements

Preparation of the working electrode. 10 mg catalyst was ground to powder and then dispersed in 1 mL mixed solvent (500 μL EtOH, 400 μL H₂O and 100 μL Nafion) by ultrasonication to form a homogeneous ink. Subsequently, 50 μL of the ink was covered onto the front side of carbon cloth (2 cm × 1 cm) and bake-dried under infrared light for measurements. In addition, the area of the coating catalyst was controlled to 0.5 cm × 1 cm. In all measurements, the loading mass of the catalyst on the carbon cloth was 1 mg cm⁻².

Electrolysis and analysis of the CO₂ reduction product. The electrocatalytic CO₂ reduction test is carried out in a typical three-electrode system using a flow cell under normal temperature and pressure. The anion exchange membrane is used as the separator, the catalyst-loaded carbon paper (CP, the actual test area is 0.25 cm²) is used as the working electrode, the Pt sheet is used as the counter electrode, the Ag/AgCl (KCl saturated) electrode is used as the reference electrode, and the 1 M KOH aqueous solution is used as the electrolyte. Before the measurement, the pure CO₂ gas stream was passed through the entire device for at least 30 minutes to remove the impurity gas in the device. The device was tested under the condition of continuous CO₂. The measured potential was converted relative to the reversible hydrogen electrode (RHE) according to the equation: $E(\text{V vs. RHE}) = E(\text{V vs. Ag/AgCl}) + 0.197 + 0.059 \times \text{pH}$.

The gaseous reduction products (*e.g.*, CO, CH₄, C₂H₄, H₂) were monitored with a gas chromatograph (GC, Agilent 7820A) equipped with a flame ionization detector (FID) and a thermal conductivity detector (TCD). The formula for calculating the Faraday efficiency (FE) of the CO₂RR is as follows:

$$j_i = x_i \times v \times (n_i \text{FP}_0 / \text{RT})$$

$$\text{FE} = (j_i / j_{\text{total}}) \times 100\%$$

Among them, x_i is the volume fraction obtained from the chromatographic standard curve; v is the gas flow rate in the flow cell, in L s^{-1} ; n_i is the number of transferred electrons of the reduction product; F is the Faraday constant, which is $96\,485\text{ C mol}^{-1}$; P_0 is a standard atmospheric pressure, which is 101.3 kPa ; R is the molar gas constant, which is $8.314\text{ Pa mol}^{-1}\text{ K}^{-1}$; T is the temperature of the test system; j_i is the partial current density of the reduction product; j_{total} is the total current density.

Liquid products (such as formate) are quantified by $^1\text{H-NMR}$. In a typical analysis, the mixture solution of $400\ \mu\text{L}$ of the electrolyte and $100\ \mu\text{L}$ of D_2O was used as the measured sample.

Other electrochemical measurements. Linear sweep voltammetry (LSV) was performed at a sweep rate of 5 mV s^{-1} . In order to estimate the electrochemically active surface area (ECSA) of the catalyst, the double-layer capacitance (C_{dl}) was calculated by testing the CV at various scan rates of $20\text{--}200\text{ mV s}^{-1}$ in the potential range of $1.05\text{--}1.15\text{ V vs. RHE}$. The electrochemical impedance spectroscopy (EIS) measurement was carried out at -1.0 V vs. RHE over a frequency range from 0.1 Hz to 1000 kHz , and a 20 mV amplitude of sinusoidal potential perturbation was employed in the measurements. The chronoamperometry was measured at the current density corresponding to a potential of -1.0 V vs. RHE . All electrochemical measurements are made with 85% iR correction.

Author contributions

Y.-Q. L., J. L., and J.-N. L. conceived and designed the idea. J.-N. L. designed the experiments, collected and analysed the data. L. Z., L.-Z. D. and S.-L. L. assisted with the experiments and characterization. J.-N. L. wrote the manuscript. J.-N. L., J. L., S.-L. L., and Y.-Q. L. discussed the results and prepared the manuscript. All the authors reviewed and contributed to this paper.

Conflicts of interest

There are no conflicts to declare.

Acknowledgements

This work was financially supported by the NSFC (Grant No. 21871141, 21871142, 92061101, and 22071109), the project funded by the China Postdoctoral Science Foundation (Grant No. 2018M630572), the Excellent Youth Foundation of Jiangsu Natural Science Foundation (No. BK20211593), the Priority Academic Program Development of Jiangsu Higher Education Institutions, and the Foundation of Jiangsu Collaborative Innovation Center of Biomedical Functional Materials.

Notes and references

- H. Furukawa, K. E. Cordova, M. O'Keeffe and O. M. Yaghi, *Science*, 2013, **341**, 1230444.
- G. R. Desiraju, *J. Am. Chem. Soc.*, 2013, **135**, 9952–9967.

- M. E. Ziebel, C. A. Gaggioli, A. B. Turkiewicz, W. Ryu, L. Gagliardi and J. R. Long, *J. Am. Chem. Soc.*, 2020, **142**, 2653–2664.
- Z. W. Jiang, Y. C. Zou, T. T. Zhao, S. J. Zhen, Y. F. Li and C. Z. Huang, *Angew. Chem., Int. Ed.*, 2020, **59**, 3300–3306.
- Q. Huang, Q. Niu, N.-N. Ma, L.-Z. Dong, S.-L. Li, D.-S. Li, Y.-P. Cai and Y.-Q. Lan, *Chem. Commun.*, 2020, **56**, 14817–14820.
- K. Sun, M. Liu, J. Pei, D. Li, C. Ding, K. Wu and H.-L. Jiang, *Angew. Chem., Int. Ed.*, 2020, **59**, 22749–22755.
- Y.-T. Xu, Z.-M. Ye, J.-W. Ye, L.-M. Cao, R.-K. Huang, J.-X. Wu, D.-D. Zhou, X.-F. Zhang, C.-T. He, J.-P. Zhang and X.-M. Chen, *Angew. Chem., Int. Ed.*, 2019, **58**, 139–143.
- Z. X. Cai, Z. L. Wang, Y. J. Xia, H. Lim, W. Zhou, A. Taniguchi, M. Ohtani, K. Kobihiro, T. Fujita and Y. Yamauchi, *Angew. Chem., Int. Ed.*, 2021, **60**, 4747–4755.
- Y.-R. Wang, R.-X. Yang, Y. Chen, G.-K. Gao, Y.-J. Wang, S.-L. Li and Y.-Q. Lan, *Sci. Bull.*, 2020, **65**, 1635–1642.
- H. Yuan, S. A. A. Aljneibi, J. Yuan, Y. Wang, H. Liu, J. Fang, C. Tang, X. Yan, H. Cai, Y. Gu, S. J. Pennycook, J. Tao and D. Zhao, *Adv. Mater.*, 2019, **31**, 1807161.
- M.-S. Yao, X.-J. Lv, Z.-H. Fu, W.-H. Li, W.-H. Deng, G.-D. Wu and G. Xu, *Angew. Chem., Int. Ed.*, 2017, **56**, 16510–16514.
- W. Cai, J. Wang, C. Chu, W. Chen, C. Wu and G. Liu, *Adv. Sci.*, 2019, **6**, 1801526.
- H. Zheng, Y. Zhang, L. Liu, W. Wan, P. Guo, A. M. Nystrom and X. Zou, *J. Am. Chem. Soc.*, 2016, **138**, 962–968.
- Q. B. Dong, X. Zhang, S. Liu, R. B. Lin, Y. N. Guo, Y. S. Ma, A. Yonezu, R. Krishna, G. P. Liu, J. G. Duan, R. Matsuda, W. Q. Jin and B. L. Chen, *Angew. Chem., Int. Ed.*, 2020, **59**, 22756–22762.
- S. Hiraide, Y. Sakanaka, H. Kajiro, S. Kawaguchi, M. T. Miyahara and H. Tanaka, *Nat. Commun.*, 2020, **11**, 3867.
- B. Moulton and M. J. Zaworotko, *Chem. Rev.*, 2001, **101**, 1629–1658.
- J.-P. Zhang, X.-C. Huang and X.-M. Chen, *Chem. Soc. Rev.*, 2009, **38**, 2385–2396.
- J. Wang, H. Zhao, M. Chen, Z. Jiang, F. Wang, D. Liu, Z. Jiang, T.-Z. Xie, Z. Zhang and P. Wang, *Chem. Commun.*, 2020, **56**, 8444–8447.
- S. Liu, Y. Huang, Q. Dong, H. Wang and J. Duan, *Inorg. Chem.*, 2020, **59**, 9569–9578.
- R.-W. Huang, X.-Y. Dong, B.-J. Yan, X.-S. Du, D.-H. Wei, S.-Q. Zang and T. C. W. Mak, *Angew. Chem., Int. Ed.*, 2018, **57**, 8560–8566.
- X. Fan, J. Wang, K. Wu, L. Zhang and J. Zhang, *Angew. Chem., Int. Ed.*, 2019, **58**, 1320–1323.
- D. N. Dybtsev, H. Chun and K. Kim, *Angew. Chem., Int. Ed.*, 2004, **43**, 5033–5036.
- Y. Yan, E. J. Carrington, R. Pétuya, G. F. S. Whitehead, A. Verma, R. K. Hylton, C. C. Tang, N. G. Berry, G. R. Darling, M. S. Dyer, D. Antypov, A. P. Katsoulidis and M. J. Rosseinsky, *J. Am. Chem. Soc.*, 2020, **142**, 14903–14913.
- C. A. Wheaton and R. J. Puddephatt, *Angew. Chem., Int. Ed.*, 2007, **46**, 4461–4463.

- 25 F. Wang, F. Gan, C. Shen and H. Qiu, *J. Am. Chem. Soc.*, 2020, **142**, 16167–16172.
- 26 I.-H. Park, R. Medishetty, J.-Y. Kim, S. S. Lee and J. J. Vittal, *Angew. Chem., Int. Ed.*, 2014, **53**, 5591–5595.
- 27 Y. Gong, Y. Zhang, C. Qin, C. Sun, X. Wang and Z. Su, *Angew. Chem., Int. Ed.*, 2019, **58**, 780–784.
- 28 J.-P. Zhang, Y.-Y. Lin, W.-X. Zhang and X.-M. Chen, *J. Am. Chem. Soc.*, 2005, **127**, 14162–14163.
- 29 M. Eddaoudi, J. Kim, N. Rosi, D. Vodak, J. Wachter, M. O’Keeffe and O. M. Yaghi, *Science*, 2002, **295**, 469–472.
- 30 L. Fan, X. Zhang, Z. Sun, W. Zhang, Y. Ding, W. Fan, L. Sun, X. Zhao and H. Lei, *Cryst. Growth Des.*, 2013, **13**, 2462–2475.
- 31 Y.-W. Huang, P.-M. Chuang and J.-Y. Wu, *Inorg. Chem.*, 2020, **59**, 9095–9107.
- 32 A. Gheorghie, I. Imaz, J. I. van der Vlugt, D. Maspoch and S. Tanase, *Dalton Trans.*, 2019, **48**, 10043–10050.
- 33 C.-P. Li and M. Du, *Chem. Commun.*, 2011, **47**, 5958–5972.
- 34 S. Tian, Y.-Z. Li, M.-B. Li, J. Yuan, J. Yang, Z. Wu and R. Jin, *Nat. Commun.*, 2015, **6**, 8667.
- 35 C. Hu and U. Englert, *Angew. Chem., Int. Ed.*, 2005, **44**, 2281–2283.
- 36 S. Masaoka, D. Tanaka, Y. Nakanishi and S. Kitagawa, *Angew. Chem., Int. Ed.*, 2004, **43**, 2530–2534.
- 37 S. Ma, D. Sun, M. Ambrogio, J. A. Fillinger, S. Parkin and H.-C. Zhou, *J. Am. Chem. Soc.*, 2007, **129**, 1858–1859.
- 38 T. Friščić, D. G. Reid, I. Halasz, R. S. Stein, R. E. Dinnebieer and M. J. Duer, *Angew. Chem., Int. Ed.*, 2010, **49**, 712–715.
- 39 Y. Ye, S. Chen, L. Chen, J. Huang, Z. Ma, Z. Li, Z. Yao, J. Zhang, Z. Zhang and S. Xiang, *ACS Appl. Mater. Interfaces*, 2018, **10**, 30912–30918.
- 40 W. Luc, B. H. Ko, S. Kattel, S. Li, D. Su, J. G. Chen and F. Jiao, *J. Am. Chem. Soc.*, 2019, **141**, 9902–9909.
- 41 W. Ma, S. Xie, T. Liu, Q. Fan, J. Ye, F. Sun, Z. Jiang, Q. Zhang, J. Cheng and Y. Wang, *Nat. Catal.*, 2020, **3**, 478–487.
- 42 T.-T. Zhuang, Z.-Q. Liang, A. Seifitokaldani, Y. Li, P. De Luna, T. Burdyny, F. Che, F. Meng, Y. Min, R. Quintero-Bermudez, C. T. Dinh, Y. Pang, M. Zhong, B. Zhang, J. Li, P.-N. Chen, X.-L. Zheng, H. Liang, W.-N. Ge, B.-J. Ye, D. Sinton, S.-H. Yu and E. H. Sargent, *Nat. Catal.*, 2018, **1**, 421–428.
- 43 D. Ren, J. Gao, L. Pan, Z. Wang, J. Luo, S. M. Zakeeruddin, A. Hagfeldt and M. Gratzel, *Angew. Chem., Int. Ed.*, 2019, **58**, 15036–15040.
- 44 J.-Y. Kim, D. Hong, J.-C. Lee, H. G. Kim, S. Lee, S. Shin, B. Kim, H. Lee, M. Kim, J. Oh, G.-D. Lee, D.-H. Nam and Y.-C. Joo, *Nat. Commun.*, 2021, **12**, 3765.
- 45 F. Ren, W. Hu, C. Wang, P. Wang, W. Li, C. Wu, Y. Yao, W. Luo and Z. Zou, *CCS Chem.*, 2021, **3**, 1670–1678.
- 46 M. S. Xie, B. Y. Xia, Y. Li, Y. Yan, Y. Yang, Q. Sun, S. H. Chan, A. Fisher and X. Wang, *Energy Environ. Sci.*, 2016, **9**, 1687–1695.
- 47 H. Zhang, X. Chang, J. G. Chen, W. A. Goddard, III, B. Xu, M.-J. Cheng and Q. Lu, *Nat. Commun.*, 2019, **10**, 3340.
- 48 L. Zhang, X.-X. Li, Z.-L. Lang, Y. Liu, J. Liu, L. Yuan, W.-Y. Lu, Y.-S. Xia, L.-Z. Dong, D.-Q. Yuan and Y.-Q. Lan, *J. Am. Chem. Soc.*, 2021, **143**, 3808–3816.
- 49 F. Li, A. Thevenon, A. Rosas-Hernandez, Z. Wang, Y. Li, C. M. Gabardo, A. Ozden, D. Cao Thang, J. Li, Y. Wang, J. P. Edwards, Y. Xu, C. McCallum, L. Tao, Z.-Q. Liang, M. Luo, X. Wang, H. Li, C. P. O’Brien, C.-S. Tan, D.-H. Nam, R. Quintero-Bermudez, T.-T. Zhuang, Y. C. Li, Z. Han, R. D. Britt, D. Sinton, T. Agapie, J. C. Peters and E. H. Sargent, *Nature*, 2020, **577**, 509–514.
- 50 C. T. Dinh, T. Burdyny, M. G. Kibria, A. Seifitokaldani, C. M. Gabardo, F. P. Garcia de Arquer, A. Kiani, J. P. Edwards, P. De Luna, O. S. Bushuyev, C. Zou, R. Quintero-Bermudez, Y. Pang, D. Sinton and E. H. Sargent, *Science*, 2018, **360**, 783–787.
- 51 L. Jiao, W. Yang, G. Wan, R. Zhang, X. Zheng, H. Zhou, S.-H. Yu and H.-L. Jiang, *Angew. Chem., Int. Ed.*, 2020, **59**, 20589–20595.
- 52 Y.-R. Wang, Q. Huang, C.-T. He, Y. Chen, J. Liu, F.-C. Shen and Y.-Q. Lan, *Nat. Commun.*, 2018, **9**, 4466.
- 53 D.-H. Nam, O. Shekhah, G. Lee, A. Mallick, H. Jiang, F. Li, B. Chen, J. Wicks, M. Eddaoudi and E. H. Sargent, *J. Am. Chem. Soc.*, 2020, **142**, 21513–21521.
- 54 H. Mistry, A. S. Varela, C. S. Bonifacio, I. Zegkinoglou, I. Sinev, Y.-W. Choi, K. Kisslinger, E. A. Stach, J. C. Yang, P. Strasser and B. R. Cuenya, *Nat. Commun.*, 2016, **7**, 12123.
- 55 S. Chen, Y. Su, P. Deng, R. Qi, J. Zhu, J. Chen, Z. Wang, L. Zhou, X. Guo and B. Y. Xia, *ACS Catal.*, 2020, **10**, 4640–4646.
- 56 J. Jiao, R. Lin, S. Liu, W.-C. Cheong, C. Zhang, Z. Chen, Y. Pan, J. Tang, K. Wu, S.-F. Hung, H. M. Chen, L. Zheng, Q. Lu, X. Yang, B. Xu, H. Xiao, J. Li, D. Wang, Q. Peng, C. Chen and Y. Li, *Nat. Chem.*, 2019, **11**, 222–228.
- 57 S. Nitopi, E. Bertheussen, S. B. Scott, X. Liu, A. K. Engstfeld, S. Horch, B. Seger, I. E. L. Stephens, K. Chan, C. Hahn, J. K. Nørskov, T. F. Jaramillo and I. Chorkendorff, *Chem. Rev.*, 2019, **119**, 7610–7672.
- 58 J.-J. Lv, M. Jouny, W. Luc, W. Zhu, J.-J. Zhu and F. Jiao, *Adv. Mater.*, 2018, **30**, 1803111.
- 59 X.-Z. Wang, M.-Y. Sun, J. Zheng, D. Luo, L. Qi, X.-P. Zhou and D. Li, *Dalton Trans.*, 2019, **48**, 17713–17717.